The Astrophysical Journal Letters, 758:L19 (6pp), 2012 October 10 doi:10.1088/2041-8205/758/1/L19

POLARIMETRIC IMAGING OF LARGE CAVITY STRUCTURES IN THE PRE-TRANSITIONAL PROTOPLANETARY DISK AROUND PDS 70: OBSERVATIONS OF THE DISK*

J. Hashimoto[1], R. Dong[2], T. Kudo[3], M. Honda[4], M. K. McClure[5], Z. Zhu[2], T. Muto[6], J. Wisniewski[7,8], L. Abe[9], W. Brandner[10], T. Brandt[2], J. Carson[10,11], S. Egner[3], M. Feldt[10], M. Fukagawa[12], M. Goto[13], C. A. Grady[14,15], O. Guyon[3], Y. Hayano[3], M. Hayashi[1], S. Hayashi[3], T. Henning[10], K. Hodapp[16], M. Ishii[3], M. Iye[1], M. Janson[2], R. Kandori[1], G. Knapp[2], N. Kusakabe[1], M. Kuzuhara[1,17], J. Kwon[1,18], T. Matsuo[19], S. Mayama[20], M. W. McElwain[14], S. Miyama[21], J.-I. Morino[1], A. Moro-Martin[2,22], T. Nishimura[3], T.-S. Pyo[3], G. Serabyn[23], T. Suenaga[1,18], H. Suto[1], R. Suzuki[1], Y. Takahashi[1,24], M. Takami[25], N. Takato[3], H. Terada[3], C. Thalmann[26], D. Tomono[3], E. L. Turner[2,27], M. Watanabe[28], T. Yamada[29], H. Takami[3], T. Usuda[3], and M. Tamura[1]

[1] National Astronomical Observatory of Japan, 2-21-1 Osawa, Mitaka, Tokyo 181-8588, Japan; jun.hashimoto@nao.ac.jp
[2] Department of Astrophysical Sciences, Princeton University, Princeton, NJ 08544, USA
[3] Subaru Telescope, 650 North A'ohoku Place, Hilo, HI 96720, USA
[4] Kanagawa University, 2946 Tsuchiya, Hiratsuka, Kanagawa 259-1293, Japan
[5] Department of Astronomy, The University of Michigan, 500 Church Street, 830 Dennison Building, Ann Arbor, MI 48109, USA
[6] Division of Liberal Arts, Kogakuin University, 1-24-2, Nishi-Shinjuku, Shinjuku-ku, Tokyo 163-8677, Japan
[7] University of Washington, Seattle, WA 98195, USA
[8] HL Dodge Department of Physics and Astronomy, University of Oklahoma, Norman, OK 73019, USA
[9] Laboratoire Hippolyte Fizeau, UMR6525, Universite de Nice Sophia-Antipolis, 28, avenue Valrose, F-06108 Nice Cedex 02, France
[10] Max Planck Institute for Astronomy, D-69117 Heidelberg, Germany
[11] Department of Physics and Astronomy, College of Charleston, 58 Coming Street, Charleston, SC 29424, USA
[12] Osaka University, 1-1, Machikaneyama, Toyonaka, Osaka 560-0043, Japan
[13] Universitäts-Sternwarte München, Scheinerstr. 1, D-81679 Munich, Germany
[14] Exoplanets and Stellar Astrophysics Laboratory, Code 667, Goddard Space Flight Center, Greenbelt, MD 20771, USA
[15] Eureka Scientific, 2452 Delmer, Suite 100, Oakland, CA 96002, USA
[16] University of Hawaii, 640 North A'ohoku Place, Hilo, HI 96720, USA
[17] Department of Earth and Planetary Science, University of Tokyo, 7-3-1 Hongo, Tokyo 113-0033, Japan
[18] Department of Astronomical Science, Graduate University for Advanced Studies (Sokendai), Tokyo 181-8588, Japan
[19] Department of Astronomy, Kyoto University, Kita-shirakawa-Oiwake-cho, Sakyo-ku, Kyoto 606-8502, Japan
[20] The Graduate University for Advanced Studies, Shonan International Village, Hayama-cho, Miura-gun, Kanagawa 240-0193, Japan
[21] Hiroshima University, 1-3-2 Kagamiyama, Higashi-Hiroshima 739-8511, Japan
[22] Department of Astrophysics, CAB-CSIC/INTA, E-28850 Torrej'on de Ardoz, Madrid, Spain
[23] Jet Propulsion Laboratory, California Institute of Technology, 4800 Oak Grove Drive, Pasadena, CA 91109, USA
[24] Department of Astronomy, University of Tokyo, Tokyo, Japan
[25] Institute of Astronomy and Astrophysics, Academia Sinica, P.O. Box 23-141, Taipei 10617, Taiwan
[26] Anton Pannekoek Astronomical Institute, University of Amsterdam, 1098-XH Amsterdam, The Netherlands
[27] Kavli Institute for the Physics and Mathematics of the Universe, The University of Tokyo, Kashiwa 227-8568, Japan
[28] Department of Cosmosciences, Hokkaido University, Sapporo 060-0810, Japan
[29] Astronomical Institute, Tohoku University, Aoba, Sendai 980-8578, Japan
Received 2012 July 2; accepted 2012 August 8; published 2012 September 24

ABSTRACT

We present high-resolution H-band polarized intensity (FWHM = 0.″11: 14 AU) and L'-band imaging data (FWHM = 0.″11: 15 AU) of the circumstellar disk around the weak-lined T Tauri star PDS 70 in Centaurus at a radial distance of 28 AU (0.″2) up to 210 AU (1.″5). In both images, a giant inner gap is clearly resolved for the first time, and the radius of the gap is ∼70 AU. Our data show that the geometric center of the disk shifts by ∼6 AU toward the minor axis. We confirm that the brown dwarf companion candidate to the north of PDS 70 is a background star based on its proper motion. As a result of spectral energy distribution fitting by Monte Carlo radiative transfer modeling, we infer the existence of an optically thick inner disk at a few AU. Combining our observations and modeling, we classify the disk of PDS 70 as a pre-transitional disk. Furthermore, based on the analysis of L'-band imaging data, we put an upper limit of ∼30 to ∼50 M_J on the mass of companions within the gap. Taking into account the presence of the large and sharp gap, we suggest that the gap could be formed by dynamical interactions of sub-stellar companions or multiple unseen giant planets in the gap.

Key words: planetary systems – polarization – protoplanetary disks – stars: individual (PDS 70) – stars: pre-main sequence

Online-only material: color figures

1. INTRODUCTION

Protoplanetary disks are believed to be the birthplaces of planets (e.g., Hayashi et al. 1985); hence, understanding the evolution of these disks guides our understanding of the process of planet formation. Disks that have substantial infrared excesses but reduced fluxes at wavelengths $\lesssim 20\,\mu$m, i.e., transitional disks (Strom et al. 1989), could be related to the early phases of planet formation (see a recent review of Williams & Cieza 2011) and are therefore particularly important for understanding how, where, and when planets form. For many transitional disks, partial inner holes or partial gaps have been directly resolved by

* Based on data collected at the Subaru Telescope, which is operated by the National Astronomical Observatory of Japan.

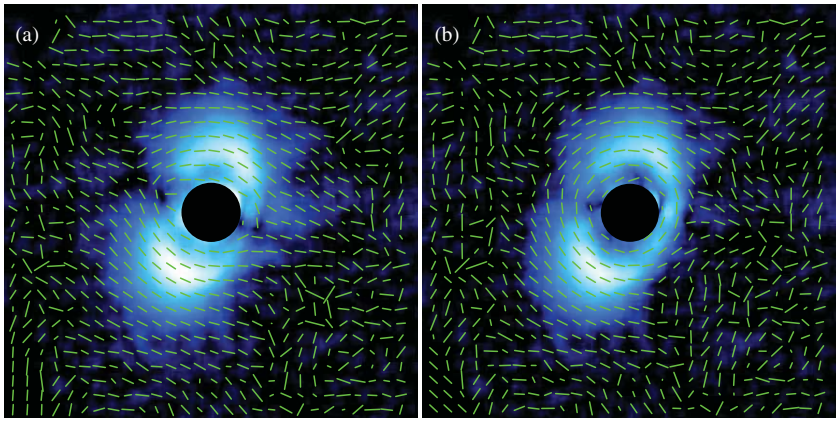

Figure 1. *H*-band polarization vectors of PDS 70 are superposed on the PI image with a software mask with 0.″4 diameter (a) before subtracting polarized halo and (b) after subtraction. The plotted vectors are binned with spatial resolution. The field of view (FOV) is 3.″0 × 3.″0. All plotted vectors' lengths are arbitrary for the presentation purposes.

(A color version of this figure is available in the online journal.)

interferometry at (sub)millimeter wavelengths (e.g., Piétu et al. 2006; Andrews et al. 2011) and imaging at near-infrared wavelengths (Fukagawa et al. 2006; Thalmann et al. 2010; Hashimoto et al. 2011). Numerous mechanisms have been proposed to explain the clearing of gaps in transitional disks, including grain growth (e.g., Dullemond & Dominik 2005), photoevaporation (e.g., Clarke et al. 2001), and gravitational interactions with orbiting planets (e.g., Papaloizou et al. 2007; Zhu et al. 2011). Two possible methods for distinguishing the disk–planet interactions from other aforementioned proposed gap-clearing mechanisms could be the detection of (1) a planetary companion in the inner hole/gap region (e.g., Kraus & Ireland 2012) or (2) a ring-like gap between optically thick inner and outer disks (i.e., pre-transitional disk; Espaillat et al. 2007) because dynamical formation of wide gaps could be the only surviving mechanism for wide gapped disks (e.g., Papaloizou et al. 2007; Zhu et al. 2011).

One good candidate to investigate the inner hole/gap region at tens of AU in pre-transitional disks is the weak-lined T Tauri star PDS 70 (K5 type, 0.82 $M_{\odot}$, <10 Myr; Gregorio-Hetem & Hetem 2002; Riaud et al. 2006; Metchev et al. 2004). A scattered light disk with a radius at 14–140 AU was detected by Ks-band imaging (Riaud et al. 2006). The possible presence of inner and outer disks with different temperatures was suggested by Metchev et al. (2004) and Riaud et al. (2006), which may imply that PDS 70 is a pre-transitional disk object. In this Letter, we present high-resolution imaging of PDS 70 with Subaru/HiCIAO and Gemini/Near-Infrared Coronagraphic Imager (NICI).

2. OBSERVATIONS AND DATA REDUCTION

2.1. H-band Polarimetry with Subaru/HiCIAO

Observations of PDS 70 were conducted with HiCIAO (Tamura et al. 2006) on the Subaru Telescope in polarized differential imaging (PDI) mode, combined with angular differential imaging (ADI) mode (Marois et al. 2006), on 2012 February 28 UT. *H*-band linear polarization images were taken under the program SEEDS (Strategic Explorations of Exoplanets and Disks with Subaru; Tamura 2009). In PDI+ADI, we employed a double Wollaston prism to split incident light into four images, each with a 5″ by 5″ field of view (FOV) with a pixel scale of 9.5 mas pixel^{-1}, to make the saturated radius as small as possible.

Polarization was measured by rotating the half-wave plate to four angular positions (in the order of 0°, 45°, 22.°5, and 67.°5). We obtained 22 full wave plate rotation cycles, taking a 15 s exposure per wave plate position. The total integration time of the polarized intensity (PI) image was 660 s. Even with a large airmass of ∼2 during observations of PDS 70, the adaptive optics (AO) system (AO188; Hayano et al. 2004) provided a stellar point-spread function (PSF) of PDS 70 with FWHM of 0.″1 in the *H* band. The angle of the total field rotation was ∼13°.

The polarimetric data were reduced with the same procedure as for Hashimoto et al. (2011) using IRAF.[30] Since the Strehl ratio of the stellar PSF of PDS 70 was ∼0.26, a stellar halo remained in the image, i.e., the PSF convolved by seeing was not perfectly corrected by the AO and partially remains. This halo appears to be polarized along the minor axis of the disks since the polarization of forward and back scattering is smaller due to the deviation from 90° in the scattering angle, and thus the stellar halo has a significant net-polarization. In other words, since the flux of a PSF convolved by seeing contains contributions from both the central star and disk, the seeing PSF might be polarized along the minor axis of a disk. To correct for this "polarized halo," we first derived the net-polarization of PDS 70 with aperture polarimetry. We then made a model of the "polarized halo" of PDS 70 by multiplying the added image of *o*- and *e*-rays by the derived polarization of $P = 0.503\% \pm 0.001\%$ with $\theta = 66.°32 \pm 0.°06$. The errors were calculated with the photometric errors, and are thus a lower limit. Finally, we subtracted the model "polarized halo" and obtained final Stokes Q and U images. Figure 1 demonstrates the subtraction of the "polarized halo."

2.2. L′-band Imaging with Gemini/NICI

We carried out ADI observations of PDS 70 in the L' band on 2012 March 31, using the NICI and the 85-element AO system (Chun et al. 2008) mounted on the 8.1 m Gemini South Telescope at Cerro Pachon, Chili. NICI utilizes a 1024 × 1024 ALADDIN InSb array with a plate scale of 18 mas pixel^{-1} and FOV of 18 × 18 arcsec.

[30] IRAF is distributed by the National Optical Astronomy Observatory, which is operated by the Association of Universities for Research in Astronomy, Inc., under cooperative agreement with the National Science Foundation.

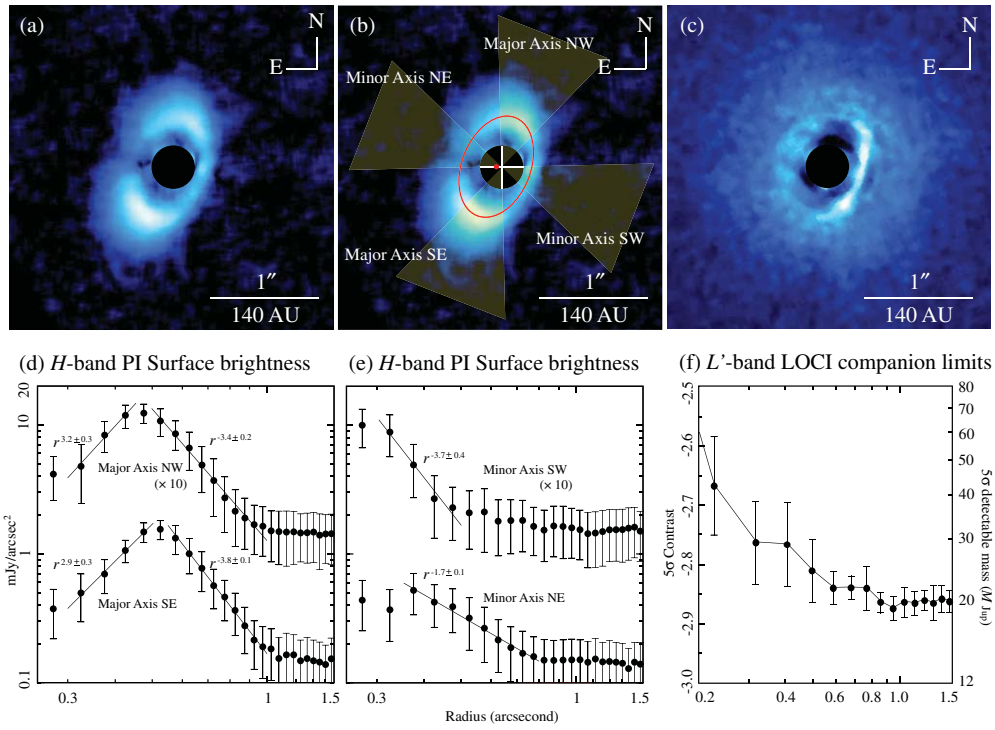

Figure 2. (a) *H*-band PI image of PDS 70 with a software mask with 0.″4 diameter. (b) Same as (a), except for its features. The solid ellipse indicates the ring-like disk. The filled circle represents the geometric center of the disk. (c) L'-band LOCI image of PDS 70 with a software mask with 0.″4 diameter. The parameters in LOCI reductions are described in Section 2.2. The FOV of three images are 3.″0 × 3.″0 with a convolution of spatial resolution. (d) and (e) Radial profiles at yellow hatched regions of the minor and major axes in (b). The values of the profile to the northwest and southwest are multiplied by 10 for the presentation purposes. (f) Detectable mass at 5σ based on the L'-band LOCI image. The LOCI parameters are same as those described in Section 2.2, but the optimization area is 250 × FWHM (N_A = 250).

(A color version of this figure is available in the online journal.)

We obtained 145 frames for PDS 70 with 0.76 s × 25 co-add for L' band. Although the sky was clear for the full night, the seeing was variable, therefore we used a subset of 95 frames, which were combined, to produce the final image. The total exposure time was 1805 s and the spatial resolution was achieved 0.″11. The angle of the total field rotation is ∼100°.

The data reduction was performed with the LOCI algorithm (Marois et al. 2006; Lafreniére et al. 2007) in annular regions of 1000 × FWHM (N_A = 1000) with reference images selected from frames with at least 0.5 × FWHM field rotation (N_δ = 0.5). A large optimization area diminishes the impact of the disk on the optimization process (Buenzli et al. 2010). The ratio of the radial and azimuthal width of the optimization area (g) is 1.

3. RESULTS AND DISCUSSION

3.1. H-band Polarimetry and L′-band Imaging

Figure 2 shows *H*-band PI images and the L'-band LOCI image of PDS 70 assuming a distance of 140 pc, along with radial surface brightness profiles. We find a clear elliptical ring in the *H* band, which has not been reported in previous high-resolution imaging (Riaud et al. 2006). A partial elliptical disk is observed in the L' band due to the inevitable loss of flux in the process of LOCI; hence, we derive radial profiles of the surface brightness based on the *H*-band PI image only and companion mass limits from the L'-band LOCI image only.

We consider that the elliptical shape is due to the system's inclination, and show the results of fitting an ellipse to these data in Table 1. The position angle of the major axis and the inclination of the disk are similar to those of K_s-band imaging (P.A. ≈ 155° and i ≈ 62°; Riaud et al. 2006). We measured an offset of 44 ± 3 mas (∼6 AU) at P.A. = 87.°9 between the geometric center of the disk and the central star. The positional accuracy of the central star is 1.5 mas (0.2 AU). The direction of this offset is roughly consistent with that of the minor axis of 68.°6, and the sign of this offset indicates that the southwest side is inclined toward us (i.e., the near side, see the model image in Dong et al. 2012b). This geometry is also consistent with the fact that (1) the northeast side of the disk is wider due to the back illumination of the wall (Thalmann et al. 2010) and (2) the southwest side is brighter than the northwest side due to forward scattering (Fukagawa et al. 2006).

Assuming that the cavity edges correspond to the peak PI of the disk, a radius of the cavity is measured as ∼70 AU. The outer radius of the disk is measured to be ∼140 AU in Figure 2(d), and corresponds to the location at which our sensitivity is no longer sufficient to detect extended emission.

A single power-law fit was performed to the radial profiles along the minor and major axes (Figures 2(d) and (e)). Our results of ∼ −3.6 and ∼ −1.7 are different from ∼ −2.8 of Riaud et al. (2006).

We also found a flux deficit of PI in the direction of the minor axis. Since the observed scattering angle at the minor axis deviates from 90°, the polarization fraction along the minor axis is lower. The PI at the minor axis is therefore lower than at the major axis, and such hole-like structures are similar to those discussed in Perrin et al. (2009).

We checked the proper motion of the companion candidate to the north of PDS 70 reported by Riaud et al. (2006). PDS 70 has

Table 1
The Results of the Ellipse and the SED Fitting for the Disk of PDS 70

Ellipse Fitting[a]	
Diameter of the major axis[b] (AU)	137.0 ± 1.1
Diameter of the minor axis[b] (AU)	88.6 ± 0.5
Position angle of the major axis (°)	158.6 ± 0.7
Inclination by ellipse fitting[c] (°)	49.7 ± 0.3
Geometric center[b,d] (AU : AU)	$(6.1 \pm 0.3 : 0.2 \pm 0.4)$
SED Fitting[e]	
$M_{\rm disk}$	0.003
f	0.967
$h_{\rm b}^{\rm o}$(100 AU)	2
$b_{\rm b}^{\rm o}$	1.2
$h_{\rm b}^{\rm c}$(100 AU)	2
$b_{\rm b}^{\rm c}$	1.2
$\delta_{\rm cav,b}$	10^{-3}
$h_{\rm s}^{\rm o}$(100 AU)	10
$b_{\rm s}^{\rm o}$	1.2
$h_{\rm s}^{\rm c}$(100 AU)	10
$b_{\rm s}^{\rm c}$	1.2
$\delta_{\rm cav,s}$	10^{-3}

Notes.
[a] In the ellipse fitting for the disk, the peak positions were first directly determined by the radial profile at position angles every 5° on the disk. We then conducted an ellipse fit using an implementation of the nonlinear least-squares Marquardt–Levenberg algorithm with five free parameters of the lengths of the major and minor axes, position angle, and central positions.
[b] We assume that the distance of PDS 70 is 140 pc.
[c] Derived from the ratio of the major and minor axes.
[d] Central position (0, 0) corresponds to the stellar position.
[e] Row 1: total mass of the disk (assuming a dust-to-gas ratio 100). Row 2: mass fraction of big dust in total dust. Rows 3, 5, 8, and 10: scale height h at 100 AU. Subscripts "b" and "s" indicate big dust and small dust, respectively. Superscripts "o" and "c" indicate outer disk and cavity, respectively. Rows 4, 6, 9, and 11: power index b in $h \propto R^b$ in various disk components. Rows 7 and 12: depletion factor of the big and small dust disk.

Table 2
Archival Photometry Data for PDS 70

Wavelength	F_ν (mJy)	Note	Plotted Color in Figure 3
U[a,b]	9.7	Gregorio-Hetem et al. (1992)	Cyan
B[a,b]	41.8	Gregorio-Hetem et al. (1992)	Cyan
V[a,b]	99.2	Gregorio-Hetem et al. (1992)	Cyan
R[a,b]	160.9	Gregorio-Hetem et al. (1992)	Cyan
I[a,b]	216.3	Gregorio-Hetem et al. (1992)	Cyan
2MASS (J)[a,b]	311.9 ± 6.9	Cutri et al. (2003)	Magenta
2MASS (H)[a,b]	342.7 ± 12.6	Cutri et al. (2003)	Magenta
2MASS (Ks)[a,b]	275.6 ± 5.8	Cutri et al. (2003)	Magenta
WISE (3.4 μm)[b]	188.1 ± 4.0	Cutri et al. (2012)	Green
WISE (4.6 μm)[b]	142.0 ± 2.6	Cutri et al. (2012)	Green
WISE (12 μm)[b]	153.9 ± 2.3	Cutri et al. (2012)	Green
WISE (22 μm)[b]	341.8 ± 0.7	Cutri et al. (2012)	Green
AKARI (9 μm)	201.2 ± 25.8	VizieR II/297	Black
AKARI (18 μm)	209.8 ± 13.4	VizieR II/297	Black
AKARI (90 μm)	851.1 ± 62.6	VizieR II/298	Black
IRAS (12 μm)	251 ± 25.1	Moshir (1989)	Blue
IRAS (25 μm)	348 ± 27.8	Moshir (1989)	Blue
IRAS (60 μm)	884 ± 61.9	Moshir (1989)	Blue
MIPS (24 μm)	$349.7^{\rm c} \pm 7.0$	*Spitzer* Heritage Archive[d]	Red
MIPS (70 μm)	$1049.9^{\rm c} \pm 19.9$	*Spitzer* Heritage Archive[d]	Red
MIPS (160 μm)	$873.0^{\rm c,e} \pm 36.2$	*Spitzer* Heritage Archive[d]	Red

Notes.
[a] An extinction law was adopted from Mathis (1990).
[b] Absolute flux conversions in optical, 2MASS, *WISE* photometric data were adopted from Bessell et al. (1998), Cohen et al. (2003), and Jarrett et al. (2011), respectively.
[c] Since photometric data were not available, we conducted aperture photometry for archival images.
[d] This work is based in part on observations made with the *Spitzer Space Telescope*, obtained from the NASA/IPAC Infrared Science Archive, both of which are operated by the Jet Propulsion Laboratory, California Institute of Technology under a contract with the National Aeronautics and Space Administration.
[e] Since the sky value was not sufficiently measured due to a small field of view of available data, our photometry may be less reliable.

a proper motion of $(\mu_\alpha \cos\delta, \mu_\delta) = (-24.7 \pm 11.4, -13.3 \pm 11.4)$ mas yr^{-1} (Roeser et al. 2010); the separation between PDS 70 and the companion candidate should increase if the companion candidate is a background star. Since the separation in HiCIAO and NICI images are 324.13 ± 0.15 AU and 324.44 ± 0.10 AU, respectively, the separation in Riaud et al. (2006) is inferred to be 309 ± 12 AU. Our estimation has good agreement with the actual observed separation of 301.75 ± 0.06 AU in Riaud et al. (2006), and therefore, we concluded that the companion candidate is a background star.

3.2. Detectable Planetary-mass Companions

Since the follow-up L'-band observations with Gemini/NICI failed to detect any significant signals of point-like sources in the gap we put constraints of upper limits for companion(s). Figure 2(f) shows the detectable masses of companions at 5σ. The LOCI parameter of the optimization area is $250 \times$ FWHM, which is different from that described in Section 2.2. For that, we first applied a median filter with $0\farcs11$ width to the image, and then calculated the standard deviation as the noise level in concentric annuli along the major axis of the disk. The mass was calculated by assuming the COND evolutionary model (Baraffe et al. 2003), a distance of 140 pc, and an age of 10 Myr (Metchev et al. 2004). We took into account the flux loss due to the partial self-subtraction by testing how point sources are affected by LOCI. The detectable mass limit is tens of $M_{\rm J}$, therefore stellar companions down to masses associated with massive brown dwarfs are excluded within the gap.

3.3. Modeling of Spectral Energy Distribution (SED)

Although the SED fitting for PDS 70 has been performed in previous studies (Metchev et al. 2004; Riaud et al. 2006), both the availability of new archival photometric data (Table 2) and our imaging results motivate us to revisit the SED of the system using Monte Carlo radiative transfer (MCRT). Note that though PDS 70 has been observed by the *Spitzer* Infrared Spectrograph (IRS), the object was mispointed by $\sim 2\farcs3$ with components along both the spatial and dispersion axes, and therefore, the IRS spectrum of PDS 70 is not used in this work.

Setup for modeling. The method for our MCRT simulations is described in Dong et al. (2012a) and B. A. Whitney et al. (2012, in preparation). In a subsequent paper (Dong et al. 2012b, hereafter Paper II), we will perform a detailed radiative transfer modeling of both the SED and the SEEDS imagery, and present a fiducial disk+cavity model which reproduces both observations well. We will also explore the parameter space around the fiducial model in Paper II, and provide a full discussion on the constraints on the various model parameters there. In this Letter, we only briefly describe the fiducial model and its resulting SED. We note that this model is not a *best*-fitting model in an

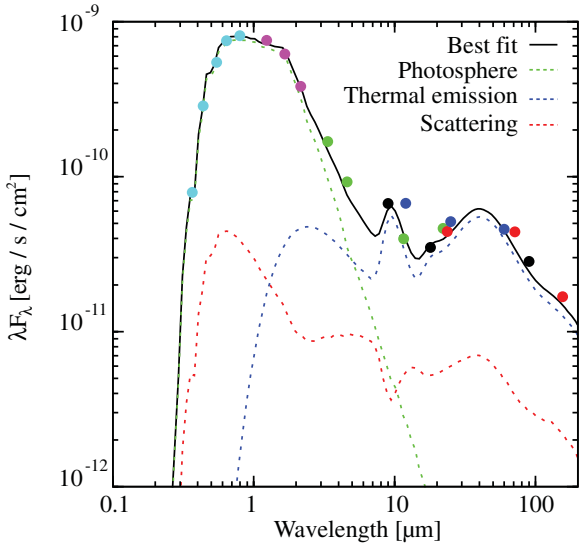

Figure 3. Pre-transitional disk model of PDS 70. Filled circles represent archival photometry (see Table 2 for photometry data). The solid black line is the best-fit model with a gap of ∼70 AU (see Table 1 for model parameters). Separate model components are as follows: stellar photosphere (green dotted line), thermal emission (blue dotted line), and scattered light (red dotted line).

(A color version of this figure is available in the online journal.)

absolute sense, since a full χ^2 fitting of the observations with all the free parameters in a protoplanetary disk is essentially impossible (Mathews et al. 2012). However, the constraints on many parameters such as the cavity size, depletion, and the surface density of the inner disk are reasonably tight, as will be shown in Paper II.

Our model contains a cavity 70 AU in radius. The surface density both inside and outside the cavity decreases with radius as $\Sigma \propto (R_c/R)e^{-R/R_c}$, where $R_c = 50$ AU, while Σ inside the cavity is reduced to $\delta\times$ the extrapolated value from the outer disk, with δ being the depletion factor. The temperature structure of the disk is determined from the radiative transfer calculations. The inner edge of the disk is self-consistently determined at the dust sublimation temperature (∼1600 K). We ignore accretion in the model, as suggested by its being a weak-lined T Tauri star (Gregorio-Hetem & Hetem 2002). We use a pre-main-sequence star of spectral type K5, radius 1.39 $R_\odot$, mass 0.82 $M_\odot$, and temperature 4500 K for the central source, as suggested by Gregorio-Hetem & Hetem (2002) and Riaud et al. (2006). The disk has a Gaussian density distribution in the vertical direction, with scale heights h as input parameters. Two disk components are included: a thick disk with small grains (sub-micron-sized), representing the pristine interstellar medium (ISM)-like dust and a thin disk with large grains (up to ∼mm-sized) and 20% of the scale height of the small grains, the result of grain growth and settling (Dullemond & Dominik 2004a, 2004b, 2005). Most of the dust mass (0.967) is in the settled disk, and the total dust-to-gas ratio is assumed to be 1/100. The SED is produced assuming a disk inclination angle of 50°. The other parameters are summarized in Table 1.

SED fitting. Figure 3 shows the good agreement between our model SED and available photometric data. As we will show in Paper II, the thermal emission from the cavity wall at ∼70 AU peaks at ∼40 μm. The wall emission is a major signature of (pre-)transitional disk SED (e.g., Espaillat et al. 2007).

The surface density of small dust is ∼0.001 g cm^{-2} at 0.1 AU, and the opacity of small dust is ∼10^4 cm^2 g^{-1} at ∼1 μm (roughly the peak of the stellar radiation). This makes the inner disk optically thick in the vertical direction. Since we assume a surface density profile decreasing with increasing radius, when moving outward, the cavity gradually becomes vertically optically thin, and the transition happens at ∼1 AU if only the small dust is taken into account (the existence of big dust inside the cavity is poorly determined from SED and scattered light image). As we will discuss in detail in Paper II, this optically thick inner disk is needed to explain the ∼2–40 μm SED, as models with an optically thin inner disk fail to reproduce the SED. Following the convention in the literature (Espaillat et al. 2007), we classify PDS 70 as a pre-transitional disk object.

3.4. Origin of the Gap

Grain growth is one mechanism that can potentially form disk gaps (e.g., Birnstiel et al. 2012). It is capable of reproducing the SED of transitional disks but not observed millimeter-wavelength images. However, the sharpness of PDS 70's H-band gap edge suggests grain growth is unlikely to be the primary reason, since the models generally predict smooth gap edge features (e.g., Birnstiel et al. 2012).

Photoevaporation is another possible mechanism. A photoevaporative wind can prevent outer disk material from feeding the inner disk; without this supply, the inner disk material will rapidly accrete onto the central star, creating a cavity inside out (Clarke et al. 2001). Although a pre-transitional disk-like structure could be produced for a very short period (see Figure 1 in Alexander et al. 2006), it is quite unlikely that such a snapshot will be observed by coincidence, and so it may be difficult to explain the existence of the optically thick inner disk inferred from the SED.

Dynamical interactions with (sub)stellar companions (e.g., Artymowicz & Lubow 1994) or orbiting planets (e.g., Papaloizou et al. 2007; Zhu et al. 2011) are also potential mechanisms, as several binary systems (e.g., CoKu Tau 4; Ireland & Kraus 2008) are known to have a cavity in their circumbinary disk, and simulations show that multiple planets can open wide gaps (Zhu et al. 2011). Furthermore, the survival of an optically thick inner disk within a few AU in Zhu et al. (2011) mimics the inner disk of PDS 70. Our L'-band observation has only ruled out companions with mass $\gtrsim 50 M_J$ in the gap region. Therefore, dynamical interactions with low-mass brown dwarfs or giant planets may be the origin of the gap. To put a further constraint of an upper limit mass, future observations, such as aperture-masking interferometric observations (e.g., Nakajima et al. 1989), which has a better contrast than LOCI imaging, should be pursued. Since PDS 70 harbors the pre-transitional disk with one of the largest gaps, this object may be one of the best candidates for future high-contrast planet imagers.

We are grateful to an anonymous referee for providing many useful comments leading to an improved version of this Letter. We appreciate support from the Subaru Telescope and the Gemini South Telescope staff, especially from Jennie Berghuis and Dr. Tom Hayward. This work is partly supported by a Grant-in-Aid for Science Research in a Priority Area from MEXT, by the Mitsubishi Foundation, and by the U.S. National Science Foundation under Award Nos. 1009203 and 1009314.

REFERENCES

Alexander, R. D., Clarke, C. J., & Pringle, J. E. 2006, MNRAS, 369, 229
Andrews, S. M., Wilner, D. J., Espaillat, C., et al. 2011, ApJ, 732, 42

Artymowicz, P., & Lubow, S. H. 1994, ApJ, 421, 651
Baraffe, I., Chabrier, G., Barman, T. S., Allard, F., & Hauschildt, P. H. 2003, A&A, 402, 701
Bessell, M. S., Castelli, F., & Plez, B. 1998, A&A, 333, 231
Birnstiel, T., Andrews, S. M., & Ercolano, B. 2012, A&A, 544, A79
Buenzli, E., Thalmann, C., Vigan, A., et al. 2010, A&A, 524, L1
Chun, M., Toomey, D., Wahhaj, Z., et al. 2008, Proc. SPIE, 7015, 49
Clarke, C., Gendrin, A., & Sotomayor, M. 2001, MNRAS, 328, 485
Cohen, M., Wheaton, W. A., & Megeath, S. T. 2003, AJ, 126, 1090
Cutri, R. M., Skrutskie, M. F., van Dyk, S., et al. 2003, 2MASS All-Sky Catalog of Point Sources, VizieR Online Data Catalog II/246
Cutri, R. M., et al. 2012, Explanatory Supplement to the WISE All-Sky Data Release Products. Technical Report, http://wise2.ipac.caltech.edu/docs/release/allsky/expsup/index.html
Dong, R., Hashimoto, J., Rafikov, R., et al. 2012b, arXiv:1209.3772 (Paper II)
Dong, R., Rafikov, R., Zhu, Z., et al. 2012a, ApJ, 750, 161
Dullemond, C. P., & Dominik, C. 2004a, A&A, 417, 159
Dullemond, C. P., & Dominik, C. 2004b, A&A, 421, 1075
Dullemond, C. P., & Dominik, C. 2005, A&A, 434, 971
Espaillat, C., Calvet, N., D'Alessio, P., et al. 2007, ApJ, 670, L135
Fukagawa, M., Tamura, M., Itoh, Y., et al. 2006, ApJ, 636, L153
Gregorio-Hetem, J., & Hetem, A. 2002, MNRAS, 336, 197
Gregorio-Hetem, J., Lepine, J. R. D., Quast, G. R., Torres, C. A. O., & de La Reza, R. 1992, AJ, 103, 549
Hashimoto, J., Tamura, M., Muto, T., et al. 2011, ApJ, 729, L17
Hayano, Y., Saito, Y., Saito, N., et al. 2004, Proc. SPIE, 5490, 1088
Hayashi, C., Nakazawa, K., & Nakagawa, Y. 1985, in Protostars and Planets II, ed. D. C. Black & M. S. Matthews (Tucson, AZ: Univ. Arizona Press), 1100
Ireland, M. J., & Kraus, A. L. 2008, ApJ, 678, L59
Jarrett, T. H., Cohen, M., Masci, F., et al. 2011, ApJ, 735, 112
Kraus, A. L., & Ireland, M. J. 2012, ApJ, 745, 5
Lafreniére, D., Marois, C., Doyon, R., Nadeau, D., & Artigau, E. 2007, ApJ, 660, 770
Marois, C., Lafreniére, D., Doyon, R., Macintosh, B., & Nadeau, D. 2006, ApJ, 641, 556
Mathews, G. S., Williams, J. P., & Ménard, F. 2012, ApJ, 753, 59
Mathis, J. S. 1990, ARA&A, 28, 37
Metchev, S. A., Hillenbrand, L. A., & Meyer, M. R. 2004, ApJ, 600, 435
Moshir, M. 1989, IRAS Faint Source Catalog, VizieR Online Data Catalog II/156A
Muto, T., Grady, C. A., Hashimoto, J., et al. 2012, ApJ, 748, L22
Nakajima, T., Kulkarni, S. R., Gorham, P. W., et al. 1989, AJ, 97, 1510
Papaloizou, J. C. B., Nelson, R. P., Kley, W., Masset, F. S., & Artymowicz, P. 2007, in Protostars and Planets V, ed. B. Reipurth, D. Jewitt, & K. Keil (Tucson, AZ: Univ. Arizona Press), 655
Perrin, M. D., Schneider, G., Duchene, G., et al. 2009, ApJ, 707, L132
Piétu, V., Dutrey, A., Guilloteau, S., Chapillon, E., & Pety, J. 2006, A&A, 460, L43
Riaud, P., Boccaletti, A., Baudrand, J., & Rouan, D. 2006, A&A, 458, 317
Roeser, S., Demleitner, M., & Schilbach, E. 2010, AJ, 139, 2440
Strom, K. M., Strom, S. E., Edwards, S., Cabrit, S., & Skrutskie, M. F. 1989, AJ, 97, 1451
Tamura, M. 2009, in Proc. Exoplanets and Disks: Their Formation and Diversity (2009 March 9–12), ed. T. Usuda, M. Ishii, & M. Tamura (Melville, NY: AIP), 11
Tamura, M., Hodapp, K., Takami, H., et al. 2006, Proc. SPIE, 6269, 28
Thalmann, C., Grady, C. A., Goto, M., et al. 2010, ApJ, 718, L87
Williams, J. P., & Cieza, L. A. 2011, ARA&A, 49, 67
Zhu, Z., Nelson, R. P., Hartmann, L., Espaillat, C., & Calvet, N. 2011, ApJ, 729, 47